MOX-Report No. 06/2022

T cell therapy against cancer: a predictive diffuse-interface mathematical model informed by pre-clinical studies

Pozzi, G.; Grammatica, B.; Chaabane, L.; Catucci, M.;

Mondino, A.; Zunino, P.; Ciarletta, P.

MOX, Dipartimento di Matematica
Politecnico di Milano, Via Bonardi 9 - 20133 Milano (Italy)

mox-dmat@polimi.it http://mox.polimi.it

T cell therapy against cancer: a predictive diffuse-interface mathematical model informed by pre-clinical studies.

G. Pozzi[1], B. Grammatica[1], L. Chaabane[2], M. Catucci[3], A. Mondino[3], P. Zunino[1], P. Ciarletta[1*]

[1] MOX Laboratory, Department of Mathematics, Politecnico di Milano, Piazza Leonardo da Vinci 32, 20133 Milano, Italy.

[2] Experimental Neurology (INSPE) and Experimental Imaging Center (CIS), Neuroscience Division, IRCCS Ospedale San Raffaele, Via Olgettina 60, 20132 Milan, Italy.

[3] Lymphocyte Activation Unit, Division of Immunology, Transplantation and Infectious Diseases, IRCCS San Raffaele Scientific Institute, Via Olgettina 60, 20132 Milan, Italy.

*Corresponding author. E-mail: pasquale.ciarletta@polimi.it

Abstract

T cell therapy has become a new therapeutic opportunity against solid cancers. Predicting T cell behaviour and efficacy would help therapy optimization and clinical implementation. In this work, we model responsiveness of mouse prostate adenocarcinoma to T cell-based therapies. The mathematical model is based on a Cahn-Hilliard diffuse interface description of the tumour, coupled with Keller-Segel type equations describing immune components dynamics. The model is fed by preclinical magnetic resonance imaging data describing anatomical features of prostate adenocarcinoma developed in the context of the Transgenic Adenocarcinoma of the Mouse Prostate model. We perform computational simulations based on the finite element method to describe tumor growth dynamics in relation to local T cells concentrations. We report that when we include in the model the possibility to activate tumor-associated vessels and by that increase the number of T cells within the tumor mass, the model predicts higher therapeutic effects (tumor regression) shortly after therapy administration. The simulated results are found in agreement with reported experimental data. Thus, this diffuse-interface mathematical model well predicts T cell behavior *in vivo* and represents a proof-of-concept for the role such predictive strategies may play in optimization of immunotherapy against cancer.

Keywords: T cell therapy, vessel activation, Cahn-Hilliard, Keller-Segel, prostate cancer, TRAMP model, MRI.

1 Introduction

Latest developments in immuno-oncology have rejuvenated the interest in active and adoptive immunotherapy. Adoptive immunotherapy with tumor-specific T cells, in particular, has become a clinical reality thanks to the possibility to deliver tumor-specific T

cells, either expanded from tumor lesions or genetically engineered with TCR or CAR specific for tumor antigens starting from the patient's peripheral blood lymphocytes. While clinical responses are now consistently observed in the case of hematologic cancers, solid tumors lag behind due to the presence of specific challenges, such as poor lymphocyte intratumoral infiltration, local immuno-suppressive mechanisms and tumor heterogeneity. In addition, difficulties in predicting on target and off target off tumor toxicity delay wider clinical use of this potent strategy. One of the most important events linked to therapeutic efficacy is T cell seeding within the tumor mass. To date, T cell fate upon *in vivo* infusion is mainly performed via *ex-vivo* blood analysis. Quantitative analysis of T cell intratumoral infiltration might instead help define efficacy of the strategy at an early stage. To this aim, non invasive imaging strategies based on magnetic resonance imaging (MRI) have been under growing consideration. Such data have the potential to inform biomathematical models of T cell responses, and offer predictive tools to evaluate patient-specific responses and inform personalized approaches.

In the last decades, much effort has been devoted to model cancer-immune system interactions at the molecular, cellular and tissue scales [1, 2]. A key contribution was initially given by Kirschner and Panetta [3], who described the temporal dynamics between tumor cells, immune-effector cells and cytokines, explaining both the short-term oscillations in tumor sizes and the long-term tumor response. Similarly, Nani and Freedman [4] derived generalized criteria for determining the efficacy of adoptive cell immunotherapy. Further approaches based on the population dynamics theory have been proposed in [5–7] based on a limited number of ordinary differential equations (ODEs). In particular, Jafarnejad et al. [8] proposed an extended system of ODE to integrate the antibody pharmaco-kinetics and immune checkpoint dynamics to mimic patients specific response to immunotherapy. A further step was taken by Lai and Friedman [9] and by Butner et

al. [10], who included in the model the spatial dynamics through the use of partial differential equations (PDE). The stochastic interactions between tumour cells and stroma was then further taken into account by using agent-based models [11]. Anti-tumour efficacy of therapies combination was also modeled using the evolutionary game theory [12]. More recently, hybrid mathematical models were found to perform well in describing putative therapies outcomes [13–15], although not taking into account relevant patient-specific features, such as anatomical tumor localization, degree of perfusion and spatial constraints on drug accessibility.

This work proposes a diffuse-interface mathematical model to simulate pre-clinical data of immunotherapy in solid tumours. We have taken advantage of knowledge based on the Transgenic Adenocarcinoma of the Mouse Prostate (TRAMP) model [16–18], which is largely used to study the underlying disease mechanisms and to test new therapies against prostate cancer [19, 20]. Recent studies have found that TRAMP mice with established adenocarcinoma can be cured by allogeneic hematopoietic cell transplantation or by autologous T cells redirected to the tumor by the genetic engineering with T cells against tumor antigens [18, 21–23]. These strategies are based on the combination of lymphodepleting strategies (that create space for infused T cells), and the transfer of fully functional tumor-specific lymphocytes (from now on referred to as T cell therapy), able to infiltrate the tumor in response to chemokine gradients. Our modeling approach thus exploits MRI images of the diseased prostate, and available knowledge on the events that regulate T cell bio-distribution *in vivo*. Our work is of timely interest as it will assist the optimization of immunotherapeutic strategies and their translation to clinical grade protocol and also help to reduce excessive use of animal tests.

The article is organized as follows. In Section 2, we describe the acquisition of MRI imaging data of the prostate of TRAMP mice needed to build the computational mesh.

In Section 3 we derive the multi-physics model and its numerical implementation from thermodynamic arguments. In Section 4, we present the main results of numerical simulations, that are finally discussed in Section 5, together with a few concluding remarks.

2 Materials and Methods

2.1 Transgenic of the prostate mouse (TRAMP) model

The Transgenic Adenocarcinoma of the Mouse Prostate (TRAMP) model [24] allows to define therapy efficacy over the course of autochthonous tumor growth. TRAMP mice express the SV40 early genes (small and large T antigens; Tag) under the control of the androgen-driven rat probasin regulatory element [25]. As a result, at puberty male mice invariably develop spontaneous prostate intraepithelial neoplasia (mPIN; week 6-12), adenocarcinoma (week 12-18), with lymph node and visceral metastasis (week 18-30), closely mimicking the human pathology [26]. Because of thymic Tag expression, high affinity Tag-specific thymocytes in TRAMP mice are deleted [27]. After puberty, overexpression of Tag within prostate epithelial cells, quantitatively similarly to other prostate-associated antigens, e.g. [28, 29], also causes the loss of responsiveness of low avidity Tag-specific T cells [30]. Thus in TRAMP mice, prostate cancer (PC) development and Tag-specific immune responses well recapitulate the tolerant status found in patients with advanced PC [31]. Heterozygous CD45.2+ C57BL/6 TRAMP mice used for this work were housed, bred and genotyped in a specific pathogen-free animal facility in accordance with the EU guidelines, and with the approval of the Institutional Ethical Committee (IACUC).

2.2 *In vivo* Imaging

In vivo MRI data were acquired using a 7-Tesla scanner (Biospec, Bruker BioSpin MRI GmbH). Mice were anesthetized with isoflurane mixed with oxygen and then placed on a warmed bed inside the volumic radiofrequency coil. Following initial scans for general anatomical localization, T2 weighted images were acquired in coronal with a fast-spin echo sequence with suitable parameters to delineate the prostate (TR/TE= 3500/40 ms, matrix = 128 x 128, FOV = 30x20 mm and thickness = 1 mm). Diffusion weighted images (DWI) were then acquired to identify prostate tumor areas, according to an echo planar image sequence with the following parameters: TR/TE = 3000/23.3 ms, 4 averages, matrix = 128x128, b values = 0, 400, 600, 800, 1000 ms). The map of the apparent diffusion coefficient (ADC) was automatically calculated from the DWI data set using the scanner software (Paravision 6, Bruker BioSpin MRI GmbH).

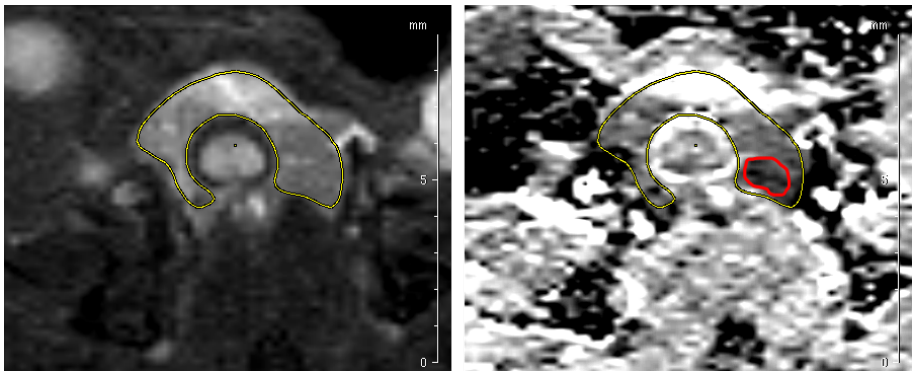

Figure 1: Example of MRI data of a TRAMP prostate. From the T2 weighted MR image (left) the whole prostate could be delimited. From the diffusion weighted images (DWI), and the corresponding map of the ADC, apparent diffusion coefficient (right), allowed the detection of the tumor area (delineated in red) in the left dorsal prostate lobe with a reduced ADC compared to healthy prostate.

3 Mathematical Model

The response to immunotherapy, in the form of T cell therapy, is modeled in the TRAMP mouse by adopting a diffuse-interface mathematical model. We first derive the system of partial differential equations governing tumor evolution under therapy. Secondly, we describe the biological parameters and the numerical scheme adopted for the *in silico* simulations.

3.1 Diffuse interface approach

The prostate is modeled as an incompressible biphasic mixture, made by the tumor, i.e. a cellular phase with volume fraction $\phi_c = \phi_c(\mathbf{x}, t)$, and the healthy host tissue, i.e. a liquid phase with volume fraction $\phi_l = \phi_l(\mathbf{x}, t)$.

We assume that the mixture is saturated, i.e. $\phi_c + \phi_l = 1$, and that the two phases have approximately the same density as the one of water, that is denoted by γ. Then, we enforce the following mass balance equation for each phase:

$$\frac{\partial \phi_i}{\partial t} + \nabla \cdot (\phi_i \boldsymbol{v}_i) = \frac{\Gamma_i}{\gamma}, \qquad i = \{c, l\} \tag{1}$$

where $\mathbf{v}_c$ and $\mathbf{v}_l$ refer to the convective velocity of the cellular and the liquid phase respectively. Moreover, we prescribe $\Gamma_c = -\Gamma_l$. Accordingly, the mixture is closed and summing the two equations (1) we obtain:

$$\nabla \cdot (\phi_c \boldsymbol{v}_c + \phi_l \boldsymbol{v}_l) = \nabla \cdot \boldsymbol{v} = 0, \tag{2}$$

which corresponds to an incompressibility constraint for the mixture velocity, that is defined as $\boldsymbol{v} = \phi_c \boldsymbol{v}_c + \phi_l \boldsymbol{v}_l$.

If we now define ϕ as the difference between the two volume fractions of the mixture, $\phi = \phi_c - \phi_l$, we can deduce the equation for the new phase field variable subtracting the two equations (1):

$$\frac{\partial(\phi_c - \phi_l)}{\partial t} + \nabla \cdot (\phi_c \boldsymbol{v}_c - \phi_l \boldsymbol{v}_l) = \frac{\Gamma_c - \Gamma_l}{\gamma}. \tag{3}$$

Then, introducing the mass fluxes of the two phases with respect to a reference system moving with the mixture velocity $\boldsymbol{v}$ [32]:

$$\begin{aligned} \boldsymbol{J}_c &= \gamma \phi_c (\boldsymbol{v}_c - \boldsymbol{v}), \\ \boldsymbol{J}_l &= \gamma \phi_l (\boldsymbol{v}_l - \boldsymbol{v}), \end{aligned} \tag{4}$$

and defining the total mass flux related to cell interactions

$$\boldsymbol{J} = \frac{1}{\gamma}(\boldsymbol{J}_c - \boldsymbol{J}_l), \tag{5}$$

we obtain the following identity:

$$\phi_c \boldsymbol{v}_c - \phi_l \boldsymbol{v}_l = \phi \boldsymbol{v} + \boldsymbol{J}, \tag{6}$$

which allows to rewrite equation (3) as:

$$\frac{\partial \phi}{\partial t} + \nabla \cdot (\phi \boldsymbol{v}) + \nabla \cdot \boldsymbol{J} = \frac{\Gamma}{\gamma}, \tag{7}$$

where $\Gamma = \Gamma_c - \Gamma_l = 2\Gamma_c$ is assumed to depend on the local concentration of oxygen.

Considering then the mixture as highly viscous and in absence of external forces, we

adopt a diffuse interface approach to find a thermodynamically consistent expression for the mass flux. First, we choose the following Helmholtz free energy for the binary mixture:

$$F(\phi) = \int_{\Omega} \left(\kappa \Psi(\phi) + \frac{\epsilon^2}{2} |\nabla \phi|^2 \right) d\Omega, \tag{8}$$

where Ω represents the volume occupied by the whole organ. The energy density in the integral accounts for cell-to-cell local interactions within each individual pure phase (healthy or diseased tissue), $\kappa\Psi(\phi)$, and the cell interactions between the two phases, through the gradient contribution representing the tension at the interface between the two phases ($|\nabla\phi|$), [33, 34]. The parameter κ instead denotes the Young modulus of the prostate, while ϵ is a parameter proportional to the thickness of the interface separating the two pure phases. To unequivocally define the free-energy, we chose a double-well form for the cell-cell interaction potential and set $\Psi(\phi) = \frac{1}{4}(1-\phi^2)^2$, so that Ψ's minima $\phi = \{-1\}$ and $\phi = \{1\}$ correspond to the two pure phases, healthy and tumor respectively. Motivated by the Fick's law, we now assume $\mathbf{J}$ to be proportional to the gradient of a chemical potential

$$\mu = \frac{\delta F(\phi)}{\delta \phi},$$

where δ indicates the Gateaux functional derivative, such that:

$$\mathbf{J} = -\frac{1}{M_0} \nabla \mu,$$

where M_0 is a friction coefficient.

To close the model, we prescribe the functional dependence of the source term Γ

appearing in (7) on the local oxygen concentration by setting

$$\Gamma = \Gamma(\phi, n) = \nu\gamma\Big(\frac{n}{n_s} - \delta\Big)h(\phi) - I(\phi, t),$$

where ν is the tumor cells proliferation rate, n is the variable describing the concentration of the oxygen, n_s is a physiological value for oxygen concentration in the capillaries, δ is the hypoxia threshold and $h(\phi) = \frac{1}{2}(1 + \phi)$ the indicator function of the tumor set. The $I(\phi, t)$ loss term in the expression for Γ, whose shape will be detailed in Section 3.2, physically represents the tumor cell death provoked by immunotherapy. Finally, we add a reaction-diffusion equation describing the spatial availability of oxygen concentration. This, for sake of simplicity, will be represented thereafter by a non-dimensional variable $\hat{n} = n/n_s$.

Thus, the system of equations describing the cancer growth in the model is:

$$\frac{\partial\phi}{\partial t} = \nabla \cdot \left(\frac{1}{M_0}\nabla\mu\right) + \nu\gamma\Big(\hat{n} - \delta\Big)h(\phi) - I(\phi, t), \tag{9}$$

$$\mu = \kappa\Psi'(\phi) - \epsilon^2\Delta\phi, \tag{10}$$

$$\frac{\partial\hat{n}}{\partial t} = \nabla \cdot (D_n\nabla\hat{n}) + S_n(1 - \hat{n})\frac{1}{3}(2 - \phi) - \delta_n\hat{n}h(\phi). \tag{11}$$

on the domain $\Omega \times [0, T]$ with $T > 0$. With Equation (11) we model the evolution of the local nutrient concentration. In particular, assuming that the vasculature within the tissue is homogeneous, we take into account the oxygen release and uptake by means of the blood vessels to the organ. We assume this process to occur at a constant rate S_n, and to be reduced in the tumor region due to proliferating tumor cells damaging the capillaries [34]. We also assume that once the oxygen is released, it diffuses in the organ

with diffusivity D_n and it is consumed by the cancer cells at rate δ_n. In addition, we assume oxygen uptake and consumption to be in equilibrium in the healthy tissue due to preserved vasculature [34]. It is worth mentioning that Equation (9) is a Cahn-Hilliard type equation with constant motility equal to the inverse of a friction parameter M_0, double-well potential and source terms. Finally, we enforce the no-flux conditions for all the three variables involved in the model, assuming that the tumor cannot grow beyond the prostate outline and oxygen can only be delivered by capillaries. The physical values of the model parameters along with the initial conditions will be discussed in Section 3 and Section 4, respectively.

3.2 Immunotherapy model

We now discuss the functional expression of the immunotherapy term $I(\phi, t)$ in Equation (9). As mentioned in Section 1, we target the proposed model to TRAMP mice subjected to T cell therapy comprised of autologous TCR engineered T-lymphocytes transferred by tail vein injection. Our purpose is to model the spatio-temporal dynamics of the distribution of injected T cells in the target organ and their interaction with cancer cells.

Driven by biological considerations, we assume that lymphocytes extravasate in the prostate, in response to tissue inflammation - proportional to the concentration of chemokines α - typically higher than the physiological level α_i in the vascular system, to then return to the blood once the chemokine gradients drops, reaching L_r concentration. We also assume that T cell extravasation into tissues and also their release is influenced by blood vessels permeability, and we defined this recruitment/retention rate as S_L [35, 36]. Once in the tissue, T lymphocytes could redistribute according to chemokine gradients, also freely diffuse. This is taken into consideration with the diffusivity coefficient D_L. Given

that T cells could proliferate to variable extents at the tumor site, we decided to neglect T cell division. Thus, we consider the T-lymphocytes concentration L to be dependent on chemokine dynamics and fully described by the following *Keller-Segel* type system:

$$\frac{\partial L}{\partial t} = D_L \Delta L - \nabla \cdot \left(\frac{\chi L}{(\beta + \alpha)^2} \nabla \alpha \right) + S_L \frac{\alpha - \alpha_i}{\alpha} [L - L_r]_+, \tag{12}$$

$$\frac{\partial \alpha}{\partial t} = D_\alpha \Delta \alpha + k_\alpha L h(\phi) - d_\alpha \alpha, \tag{13}$$

where $[\,]_+$ denotes the positive part of its argument. It is important to remark that the inflammation-sensitive form of the chemotactic coefficient $\frac{\chi L}{(\beta+\alpha)^2}$ in Equation (12) models the interaction between the chemokines and their receptors on the T lymphocytes. The term is non-linear as we meant to model the influence of chemokines concentration on cell migration [37]: data indicate that in the presence of high chemokines concentrations, T cells no longer respond to chemokine gradients because of receptor desensitization [38]. Equation (13) governs the spatio-temporal evolution of the chemokines concentration. It should be considered that tumor-specific engineered T-lymphocytes promote local chemokine upregulation by the secretion of inflammatory cytokines [39]. Here D_α is the chemokines diffusivity coefficient, while k_α and d_α are their production and decay rate, respectively. No-flux conditions for the chemokines and lymphocytes concentration are enforced at the domain boundary.

Since tumor mass reduction is an index of T cell therapy efficacy, following [40–42] we model the contribution of immunotherapy with the following loss term in Equation (9):

$$I(\phi, t) = k_f(t) h(\phi) = d \frac{\hat{L}^\lambda}{s\hat{V} + \hat{L}^\lambda} h(\phi), \tag{14}$$

where $k_f(t)$ takes into account tumor rejection (physical elimination of the tumor cells).

Here, $\hat{L} = L/L_i$ where L_i is the critical T-lymphocytes concentration associated to optimal anti-tumor responses. The term $s\hat{V} = sV/V_0$, on the other hand, accounts for the tumor dimension and depends linearly on the actual tumor volume $V = V(t) = \int_\Omega h(\phi(x,t))\, dV$ and initial tumor volume V_0, through a steepness coefficient s. The latter refers to the intrinsic ability of lymphocytes to react to tumors, which is influenced by tumor size and geometry: the smaller is the value of s, the more effective is the therapy outcome. In addition, d and λ are morphology-dependent parameters describing the velocity of the lysis process. Thus s, d and λ jointly influence the tumor behavior at given cell concentration and tumor volume.

3.3 Biological parameters

The choice and the calibration of equations parameters is of utmost importance for both having realistic simulations and translating the outcomes into clinical settings. In the present work all the parameters are either taken from available pertinent literature or estimated through physical relations wherever possible. In this section, we report the range values for each parameter in the model subdivided according to their biological significance. The values related to tumor free-growth, local immune-system dynamics and tumor elimination are reported in Table 1, Table 2 and Table 3, respectively. Where the value/range could not be derived from pertinent literature or inferred, it was set in order to fit the experimental outcomes.

It should be noted that L_i represents the threshold value for T-lymphocytes counts needed for tumor regression, indicative of therapy efficacy, and it was estimated by dividing the two-dimensional cell density reported in [18] by the cell diameter, i.e. 10-15 μm [43].

	Parameter description	Value	Ref or formula
ν	Tumor cells proliferation rate	0.17 - 0.25 day^{-1}	[44]
M_0	Tumor inter-phase friction	1.37 - 3.99 (kPa·day)/mm^2	[45]
r	Tumor cell radius	0.01 mm	[46]
χ	Tumor interstitial fluid pressure	1553.2 Pa	[47]
ϵ	Diffuse interface thickness	0.79 mm·$\sqrt{\text{Pa}}$	$2\text{r}\sqrt{\chi}$
κ	Prostate Young modulus	$6.227 \cdot 10^4$ Pa	[48]
δ	Hypoxia threshold	0.15	[49]
D_n	Oxygen diffusion coefficient	155.52 mm^2/day	[49]
l_n	Oxygen penetration distance	0.1 mm	[50]
δ_n	Oxygen consumption rate	15552 day^{-1}	D_n/l_n^2
n_s	Oxygen concentration in vessels	0.07 mM	[51]
S_n	Oxygen supply rate	10^4 day^{-1}	[52]

Table 1: Values or ranges of values for the physical parameters in the tumor model.

	Parameter description	Value	Ref
D_L	Lymphocytes diffusion coefficient	$7 \cdot 10^{-3}$ mm^2/day	[53]
χ	Lymphocytes chemotactic coefficient	$2 \cdot 10^1$ molecules/(mm·day)	[-]
β	Sensitivity function parameter	10^3 molecules/mm^3	[-]
S_L	Lymphocytes release/uptake rate	0.08 - 0.45 day^{-1}	[-]
α_i	Inflammation threshold	$6.022 \cdot 10^2$ molecules/mm^3	[-]
L_r	Lymphocytes reference value	$5 \cdot 10^2$ cells/mm^3	[-]
D_α	Chemokines diffusion coefficient	0.01 - 1 mm^2/day	[53]
k_α	Chemokines production rate	$2.88 \cdot 10^4$ - $4.32 \cdot 10^6$ molecules/(cells·day)	[53]
d_α	Chemokines consumption rate	$1.155 \cdot 10^{-2}$ day^{-1}	[53]

Table 2: Values or ranges of values related to the local immune-system dynamics.

	Parameter description	Value	Ref
d	Saturation level of fractional tumor cell kill	1.43 - 7.9 day^{-1}	[40–42]
λ	Exponent of fractional tumor cell kill	0.12 - 0.9	[40–42]
s	Steepness coefficient of fractional tumor cell kill	0.14 - 5.07	[40–42]
L_i	Critical T cell concentration	$4 \cdot 10^4 - 6 \cdot 10^4$ cells/mm^3	[18]

Table 3: Ranges of values referred to the tumor lysis process by means of the therapy.

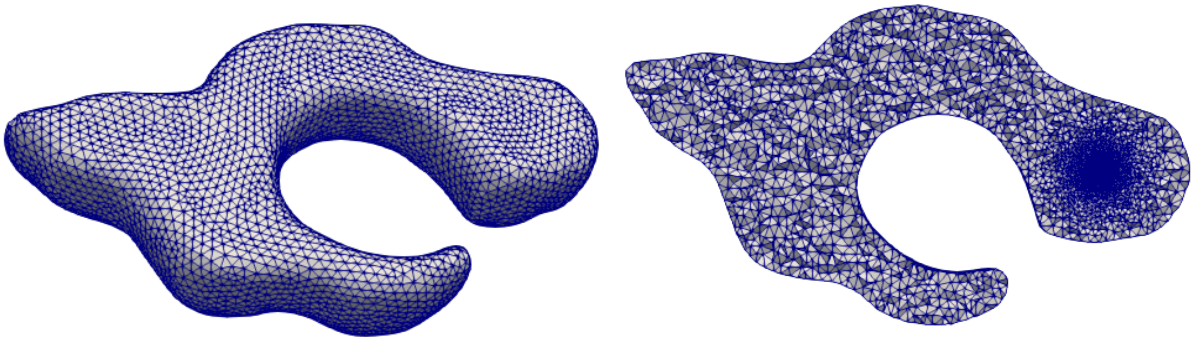

Figure 2: (Left) External prostate surface mesh extracted form MRI. (Right) Axial inner slice of the mesh with the refinement in the tumor region.

3.4 Numerical framework

Numerical simulations are obtained by the library FEniCS for solving partial differential equations using finite element methods [54, 55]. The mesh of the prostate is generated by processing pre-clinical MRI data acquired according to the protocol detailed in Section 2.

From the T2 MRI sequence we obtained a segmented map of the organ and we generated a computational mesh reproducing the mouse prostate by applying smoothing filters[56, 57]. Then, we identified the tumor position from the diffusion-weighted sequences and we refined the mesh in the surrounding area assuming the tumor to be spherical for sake of simplicity. The obtained unstructured mesh contains about 10^5 tetrahedra and it is illustrated in Figure 2.

Besides the domain partition in tetrahedral elements, which we later refer to as $\mathcal{T}_h$, we introduce the partition of the time interval [0,T] in N discrete sub-intervals $\Delta t = T/N$, thus defining the n-th simulation time-point $t^n = n\Delta t$ with $n = 0, .., N$. Within this framework, we introduce the following finite element space:

$$V_h = \{\chi \in C^0(\bar{\Omega}) : \ \chi|_{K_j} \in \mathcal{P}^1(K_j) \ \forall K_j \in \mathcal{T}_h\} \subset H^1(\Omega),$$

where $\mathcal{P}^1(K_j)$ denotes the space of polynomials of order one on the tetrahedron K_j and $H^1(\Omega)$ is an Hilbert space containing $L^2(\Omega)$ functions whose weak derivatives of order up to 1 belong to $L^2(\Omega)$.

Thus, starting from a set of initial data $(\phi_h^0, n_h^0, L_h^0, \alpha_h^0) \in V_h \times V_h \times V_h \times V_h$ the fully discrete problem reads as follows:

for n = 1,...,N

find $(\phi_h^{n+1}, \hat{n}_h^{n+1}, L_h^{n+1}, \alpha_h^{n+1}) \in V_h \times V_h \times V_h \times V_h$

such that $\forall (\varphi_h, q_h, p_h, r_h) \in V_h \times V_h \times V_h \times V_h$:

$$\Big(\frac{\alpha_h^{n+1} - \alpha_h^n}{\Delta t}, p_h\Big) = -D_\alpha(\nabla \alpha_h^{n+1}, \nabla p_h) + k_\alpha(L_h^n h(\phi_h^n), p_h) - d_\alpha(\alpha_h^{n+1}, p_h) \tag{15}$$

$$\begin{aligned}\Big(\frac{L_h^{n+1} - L_h^n}{\Delta t}, r_h\Big) = &- D_L(\nabla L_h^{n+1}, \nabla r_h) + \chi\left(\frac{L_h^{n+1}}{(\beta + \alpha_h^{n+1})^2}\nabla \alpha_h^{n+1}, \nabla r_h\right) \\ &+ S_L\left(\frac{\alpha_h^{n+1} - \alpha_i}{\alpha_h^{n+1}}[L_h^n - L_r]_+, r_h\right).\end{aligned} \tag{16}$$

$$\begin{aligned}\Big(\frac{\phi_h^{n+1} - \phi_h^n}{\Delta t}, \varphi_h\Big) = &- \frac{1}{M_0}(\nabla \mu_h^{n+1}, \nabla \varphi_h) + \nu((\hat{n}_h^{n+1} - \delta)h(\phi_h^n), \varphi_h) \\ &- d\Big(\frac{(L_h^{n+1}/L_i)^\lambda}{sV^n/V^0 + (L_h^{n+1}/L_i)^\lambda} h(\phi_h^n), \varphi_h\Big),\end{aligned} \tag{17}$$

$$(\mu_h^{n+1}, v_h) = \epsilon^2(\nabla \phi_h^{n+1}, \nabla v_h) + \kappa(\Psi_c'(\phi_h^{n+1}), v_h) + \kappa(\Psi_e'(\phi_h^n), v_h), \tag{18}$$

$$\begin{aligned}\Big(\frac{\hat{n}_h^{n+1} - \hat{n}_h^n}{\Delta t}, q_h\Big) = &- D_n(\nabla \hat{n}_h^{n+1}, \nabla q_h) + S_n\Big((1 - \hat{n}_h^{n+1})\frac{1}{3}(2 - \phi_h^n), q_h\Big) \\ &- \delta_n(\hat{n}_h^{n+1} h(\phi_h^n), q_h),\end{aligned} \tag{19}$$

where $(\cdot, \cdot)$ denotes the standard L^2 inner product over Ω and we prescribe the following splitting for the Cahn-Hilliard potential:

$$\Psi_c(\phi_h^{n+1}) = \frac{(\phi_h^{n+1})^4 + 1}{4}, \quad \Psi_e(\phi_h^n) = -\frac{(\phi_h^n)^2}{2},$$

to ensure the gradient stability of the scheme [58]. It should be noted that the Keller-Segel-type system, representing the coupled evolution of lymphocytes and chemokines, is subject to a pathological unbounded aggregation process, which leads to a blow-up of the solution. This problem is partially overcome by properly choosing the chemotactic sensitivity function in Equation (12). Nonetheless, this correction alone cannot avoid the occurrence of negative values for lymphocyte/chemokine concentrations in some regions of the domain. Thus, following [59–62], we also adopt a positivity-preserving finite element scheme to avoid non-physical numerical oscillations.

4 Results

In this Section, we present the results obtained by the numerical simulations of the mathematical model introduced in Section 3. We first discuss the initial data given as input to the model and we later evaluate responses to different immunotherapy scenarios.

4.1 Initial data

We assume that the tumor can be roughly approximated by a spherical shape and we extract from the DWI sequences the coordinates $\mathbf{x}_c$ of the tumor center and the approximate radius $\mathbf{r}_c$. We define $T_0 = \{\mathbf{x} : (\mathbf{x}-\mathbf{x}_c)^2 < \mathbf{r}_c^2\}$ as the tumor region at the initial time and we set $\phi_0(\mathbf{x}) = \phi(\mathbf{x}, t=0) = 1 \ \forall \mathbf{x} \in T_0$ and $\phi_0(\mathbf{x}) = \phi(\mathbf{x}, t=0) = -1 \ \forall \mathbf{x} \in \Omega \setminus \{T_0\}$. Hence, we model a virtual adenocarcinoma of 0.1 mm^3 located in the left dorsal lobe of the mouse prostate. The initial oxygen distribution $\hat{n}_0(\mathbf{x}) = \hat{n}(\mathbf{x}, t=0)$ is obtained by solving the steady-state version of the Equation (11), thus following the spatial distribution of ϕ_0, as depicted in Figure 3.

Furthermore, for the sake of simplifying the biological reality, we define a gaussian

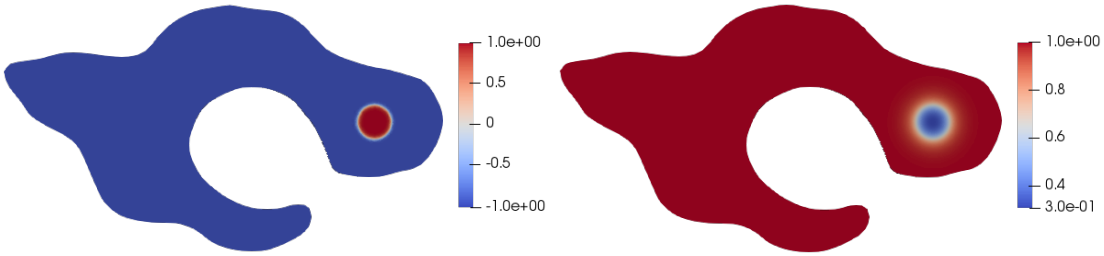

Figure 3: Axial slices of the phase field ϕ_0 (left) and nutrient n_0 (right) at the initial time step.

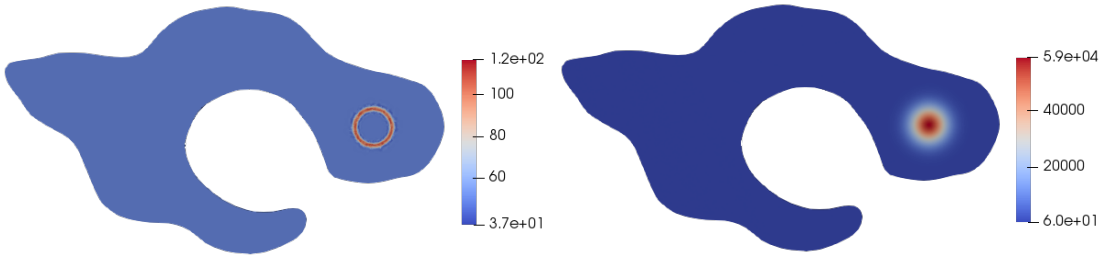

Figure 4: Axial slices of the lymphocytes L_0 (left) and chemokines α_0 (right) concentration at the initial time step.

distribution in space as the initial condition for chemokine concentrations. i.e. $\alpha_0(\mathbf{x}) = \alpha(\mathbf{x}, t = 0) = a \exp(b^{-2}(\mathbf{x} - \mathbf{x}_c)^2)$, with $a = 6.022e + 04$ molecules/mm^3 and $b = \sqrt{0.09}$ mm. Thereby, the peak of the concentration is artificially located at the tumor center and the gradient promoting cell recruitment in the neighboring area. At the same time, we assume that T cells are mainly located in a thin ring surrounding the peripheral tumor area [63]. Indeed, although they are attracted by tumor-derived inflammatory signals due to limited infiltration, they generally react to the tumor at its boundaries, i.e. the most peripheral ring [64]. Thus we impose $L_0(\mathbf{x}) = L(\mathbf{x}, t = 0) = c\mathbb{1}(T_\delta)$, where $c = 1.2e + 02$ cells/mm^3 and $T_\delta = \{\mathbf{x} : ||(\mathbf{x} - \mathbf{x}_c)^2 - \mathbf{r}_c^2|| < \boldsymbol{\delta}\}$ with $\boldsymbol{\delta} \ll \mathbf{r}_c^2$, see Figure 4.

4.2 Simulation of responses to combined immunotherapeutic approaches

Limited T cell infiltration into the tumor mass, especially in the case of solid tumors, hinders therapeutic effects of current T cell-based therapies. To overcome this hurdle, agents able to normalize the tumor associated vessel and increase vessel permeability (vessel activation) have been used by us and others [22, 35, 65]. Data support the notion that this strategy improves T cell representation and infiltration within the tumor mass, correlating with superior anti-tumor therapeutic activity [18, 21–23]. Thus, in modeling *in silico* putative responses, we consider three treatment modalities in Figure 5: (a) none, or (b) T cell therapy at day 0, or (c) T cell therapy combined with an agent able to activate tumor-associated vessel (vessel activation) at day 0. Of these strategies only the latter has curative potential [22, 23].

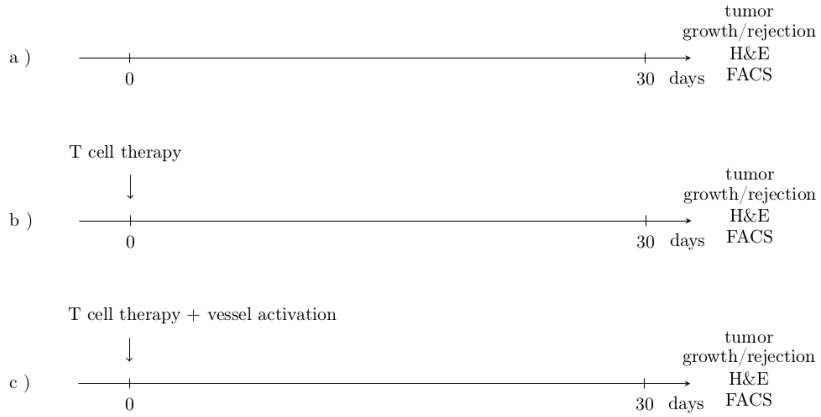

Figure 5: Treatment options: a) none; b) T cell therapy; c) T cell therapy + vessel activation.

We depict in Figure 6 (left) the curves of the tumor volume within 30 days from therapy administration. Qualitatively different responses are found when T cell therapy

and vessel activation are combined with respect to T cell therapy alone. Of note, in the presence of vessel activation, the number of lymphocytes infiltrating the tumor increases at earlier times compared to controls reaching a critical threshold correlating with tumor shrinkage Figure 6 (right). The different scenarios are reproduced with the same set of initial data and parameters except for the value of the lymphocytes release rate S_L, which is set in the range 0.08-0.15 day^{-1} in case of T cell therapy alone and in the range 0.25-0.45 day^{-1} in presence of vessel activation. Indeed, higher values of S_L mimic the role of vessel activation, able to promote lymphocyte extravasation into the tumor micro-environment.

The numerical simulations show that the tumor volume is slighter slower in the T cell therapy scenario compared to the control one, although no signs of tumor disappearance is evident. When T cell therapy and vessel activation are combined, an inversion of the tumor growth curve is observed leading complete tumor debulking. The same trends are visible also from the axial slice in Figure 7.

When considering the intratumoral pattern of lymphocytes and chemokines, shown in Figure 8, it appears qualitatively similar in the case of T cell therapy without or with vessel activation. However, the intratumoral lymphocytes concentration increases in time most significantly in the case T cell therapy and vessel activation are combined, see Figure 9. This is also evidenced by the thickening of a peripheral ring made of infiltrating T cells within the tumor, which is paralleled by a reduction in the tumor volume (respectively depicted in Figure 9 and Figure 6).

Thereby, the model exhibits a threshold behavior with respect to a critical T cell concentration: when T cells remain below a certain number therapeutic effects remain suboptimal, instead above the defined threshold infiltrating cells correlate with tumor eradication. From the trends reported in Figure 6 (right), the above mentioned critical value is estimated in the range $1 \cdot 10^4 - 2.5 \cdot 10^4$ cells/mm^3, found at the time the curves

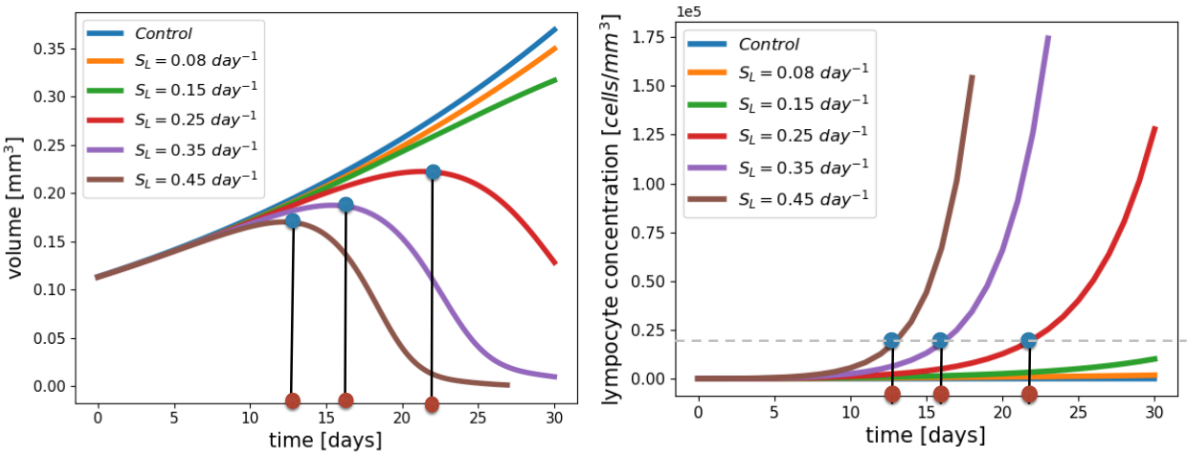

Figure 6: Temporal evolution of the tumor volume (left) and of the associated maximum value of lymphocytes concentration (right) for distinct therapeutic scenarios: (blue) the free growth in absence of therapy - case a), (orange and green) T cell therapy - case b) and (red, purple and brown) T cell therapy with vessel activation - case c), with the corresponding values of lymphocyte release rate (S_L) shown in the legend. The blue circles indicate the curve values at the initial times (red circles) of growth inversion.

associated with beneficial therapeutic outcomes present the elbow (red and blue spots). We notice that the numerical range for the threshold value is coherent with that found in treated prostate of TRAMP mice correlating with tumor rejection [18].

5 Discussion and concluding remarks

In vivo trials have shown that T cell therapy can be an effective immunotherapeutic strategy for treating cancer. In this work we propose a new mathematical tool to predict responses in pre-clinical T cell-based approaches. The partial differential model is derived from thermodynamic principles within the framework of the mixture theory. It is based on a non-degenerate Cahn-Hilliard equation with a double well potential describing the tumor evolution coupled with a reaction diffusion equation for the oxygen concentration and a Keller-Segel type system describing the immune-system exchanges. The interaction

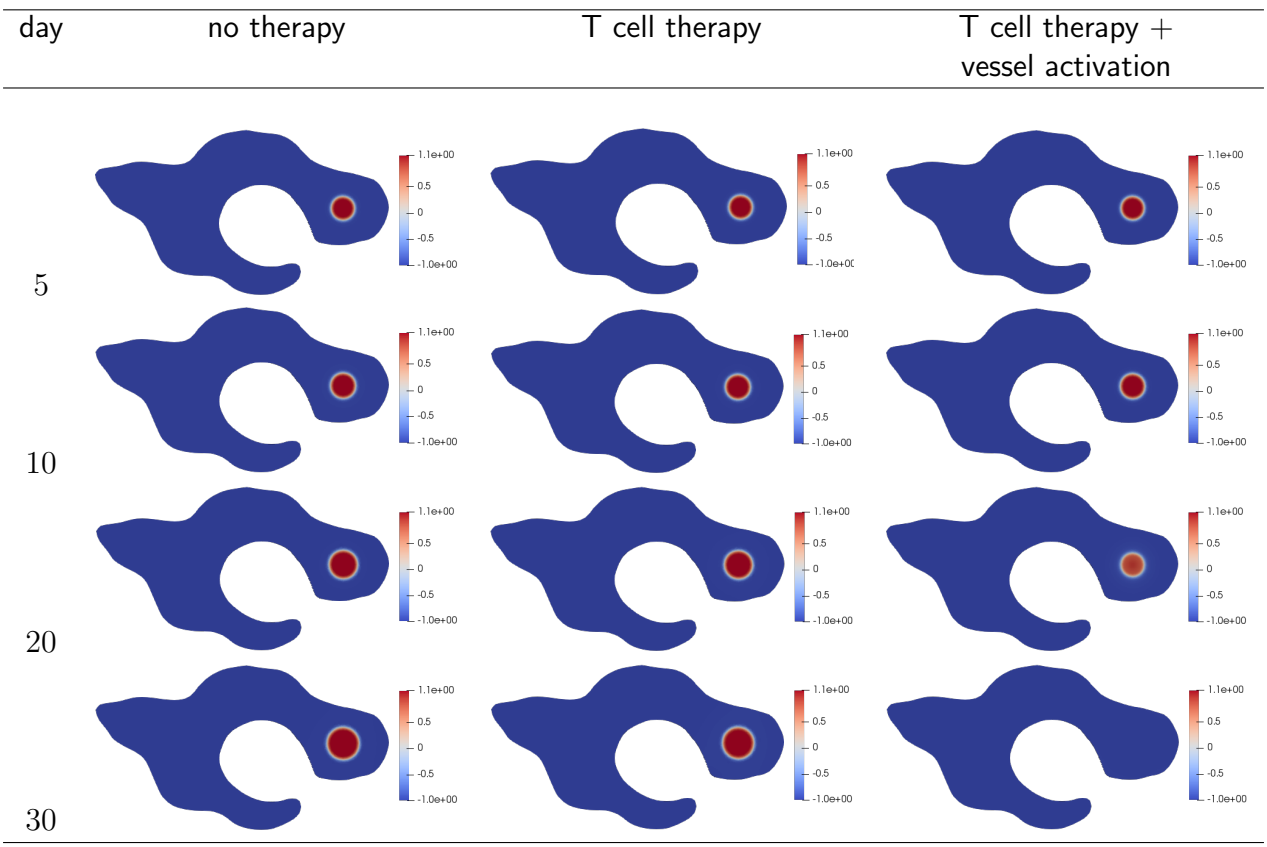

Figure 7: Axial slices representing tumor evolution in time within different scenarios: (left) no therapy; (center) T cell therapy where $S_L = 0.08$ day^{-1}; (right) T cell therapy combined with vessel activation where $S_L = 0.35$ day^{-1}.

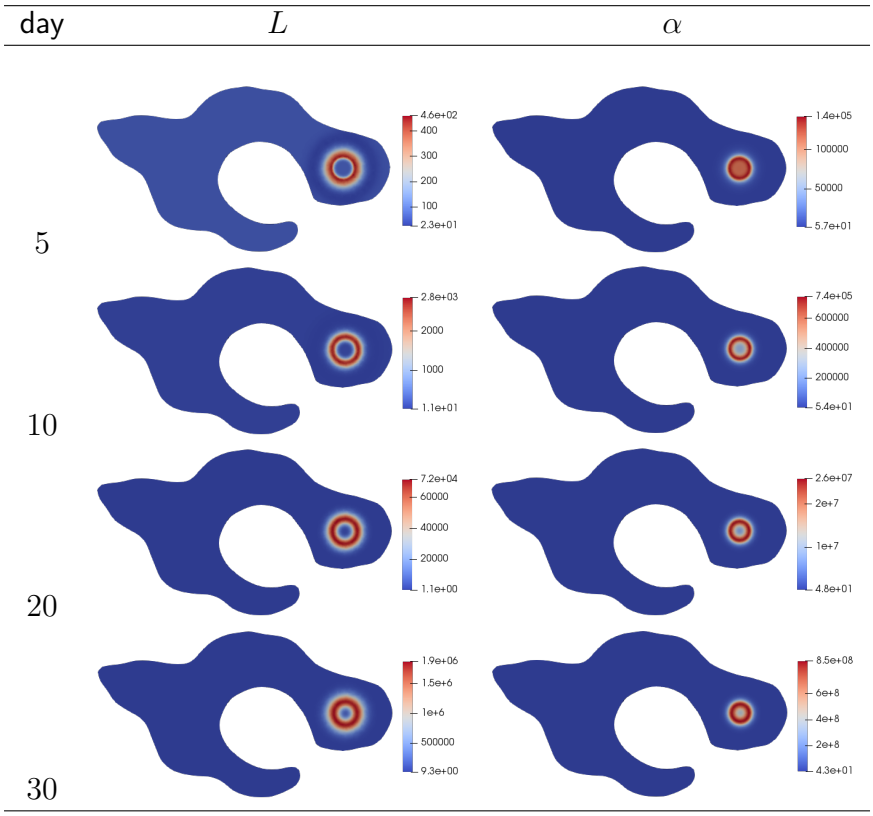

Figure 8: Lymphocytes and chemokines evolution at different time steps ($S_L = 0.35$ day^{-1}).

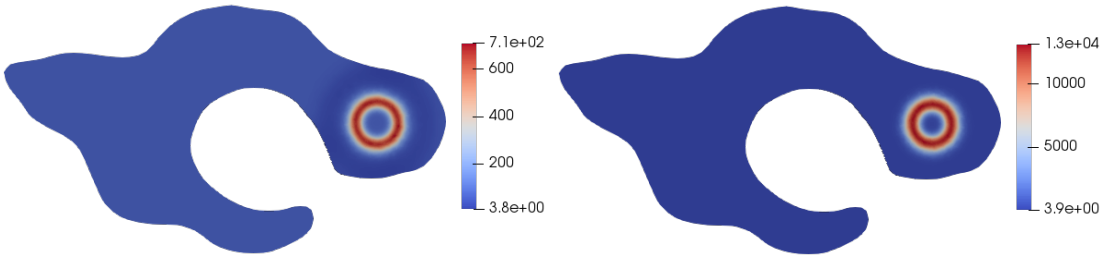

Figure 9: Lymphocytes concentration at t = 15 days (left) for the scenario of T cell therapy where $S_L = 0.08$ day^{-1}, (right) for the scenario T cell therapy combined with vessel activation where $S_L = 0.35$ day^{-1}.

between the tumor cells and the T cells is modeled through a Michaelis-Menten term. In addition, we include T cell extravasation from the blood and intratumoral infiltration to model effects of vessel activation.

The model is numerically discretized and computationally solved by using the finite element method on a virtual geometry of the mouse prostate reconstructed from MRI images. Moreover, the initial geometry of the tumor is extracted from the diffusion-weighted images with the assumption of a spherical tumor shape. Accordingly, we have performed and discussed *in silico* simulations of three different scenarios: 1) tumor growth without therapeutic intervention, 2) in the presence of T cell therapy and 3) in the presence of T cell therapy followed by vessel activation.

The numerical simulations are qualitatively in agreement with reported experimental results [18]. Indeed, considering a time lapse of 30 days, the tumor continues to grow in absence of therapy, whereas it reveals sensitive to T cell therapy according to the absence or the presence of vessel activation. In accordance with previously published data, our model reproduces the dependence of therapy efficacy on intratumoral T cell concentration. Indeed, as pre-clinical trials indicated that the number of lymphocytes can be modulated by tuning blood vessel activation and permeability, also varying the lymphocytes release rate in the numerical model resulted in higher T cell accumulation within the tumor. As a matter of fact, if we consider an improved ability of the vessels to deliver a sufficiently high number of T cells, model results show higher tumor rejection a few weeks from therapy administration.

This work can be intended as a proof-of-concept for exploiting mathematical models in support of investigations centered on T cell-based therapies. Indeed it offers a tool to predict therapy outcome and thus optimize and speed up the development of therapeutic protocols. Our simulation results suggest that a good modulation of the tumor micro-

environment promotes the lymphocytes delivery within the tumor mass. Moreover, the model highlights a threshold behavior of therapy efficacy with respect to the number of T cells that are able to reach the target organ. The numerical threshold value found in Section 4 is in line with that experimentally validated to result in tumor disappearance [18]. In the next future, we aim to enrich the model by including anisotropy in tumor expansion and in nutrient diffusion, thus taking into account diffusion tensor imaging data. We also aim to calibrate and to validate the model results against a larger experimental data set of pre-clinical trials on TRAMP mice.

In conclusion, this work represents a seminal step towards the creation of a computational tool, which integrates modeling, imaging and pre-clinical data, and supports the development of more efficient immunotherapy against cancer. This tool might support pre-clinical development of new approaches, and minimize the use of experimental animals. In addition, in association with longitudinal MRI-based patients follow up studies, it could help clinicians to tailor T cell based approaches to single patients, also minimizing unwanted therapy's side effects.

Authorship contribution statement

PC, PZ, LC and AM: conceptualization, supervision and methodology; LC and MC: Data curation; GP, BG, MC: Formal analysis; GP, LC, AM and PC: Funding acquisition; GP, BG, and PZ: Software; All authors contributed to writing, review and editing.

Acknowledgements

We are thankful to Tamara Canu (preclinical imaging facility, IRCCS Ospedale San Raffaele) for the MRI data acquisition and technical support. This work was supported by MUR PRIN 2017 grant 2017KL4EF3, by Regione Lombardia project NEWMED (Grant No. POR FESR 2014-2020) and partly by GNFM – INdAM through the program *Progetto Giovani 2020* and by AIRC to AM (AIRC IG 2018 Id 21763). MC was supported by Fondazione Umberto Veronesi.

References

[1] F. Mpekris et al. “Combining microenvironment normalization strategies to improve cancer immunotherapy.” In: *Proceedings of the National Academy of Sciences* 117.7 (2020), pp. 3728–3737.

[2] J. D. Martin et al. “Improving cancer immunotherapy using nanomedicines: progress, opportunities and challenges.” In: *Nature Reviews Clinical Oncology* 17.4 (2020), pp. 251–266.

[3] D. Kirschner and J. C. Panetta. “Modeling immunotherapy of the tumor-immune interaction.” In: *Journal of Mathematical Biology* 37 (Sept. 1998), pp. 235–252.

[4] F. Nani and H. I. Freedman. “A mathematical Model of Cancer Treatment by Immunotherapy.” In: *Mathematical Biosciences* 163 (Mar. 2000), pp. 159–199.

[5] F. Castiglione and B. Piccoli. “Cancer immunotherapy, mathematical modeling and optimal control.” In: *Journal of theoretical biology* 247 (2007), pp. 723–732.

[6] L. Barros, B. Rodrigues, and R. Almeida. “CAR-T cell Goes on a Mathematical Model.” In: *Journal of Cellular Immunology* 2 (2020), pp. 31–37.

[7] S. Nakaoka. “Mathematical analysis and classification of tumor immune dynamics in T cell transfer treatment.” In: *Nonlinear Theory and Its Applications, IEICE* 6 (2015), pp. 54–70.

[8] M. Jafarnejad et al. “A Computational Model of Neoadjuvant PD-1 Inhibition in Non-Small Cell Lung Cancer.” In: *The AAPS Journal* 21 (Sept. 2019).

[9] X. Lai and A. Friedman. “Combination therapy of cancer with cancer vaccine and immune checkpoint inhibitors: A mathematical model.” In: *PLoS ONE* 12 (May 2017).

[10] J. Butner et al. “Mathematical prediction of clinical outcomes in advanced cancer patients treated with checkpoint inhibitor immunotherapy.” In: *Science Advances* 6 (May 2020), eaay6298.

[11] J. N. Kather et al. “In Silico Modeling of Immunotherapy and Stroma-Targeting Therapies in Human Colorectal Cancer.” In: *Cancer Research* 77.22 (Nov. 2017), pp. 6442–6452.

[12] J. West et al. “The Immune Checkpoint Kick Start: Optimization of Neoadjuvant Combination Therapy Using Game Theory.” In: *JCO Clinical Cancer Informatics* 3 (Feb. 2019), pp. 1–12.

[13] C. Gong et al. “A computational multiscale agent-based model for simulating spatio-temporal tumour immune response to PD-1 and PD-L1 inhibition.” In: *Journal of The Royal Society Interface* 14 (Sept. 2017), p. 20170320.

[14] M. Benchaib et al. “Mathematical Modeling Reveals That the Administration of EGF Can Promote the Elimination of Lymph Node Metastases by PD-1/PD-L1 Blockade.” In: *Frontiers in Bioengineering and Biotechnology* 7 (May 2019).

[15] L. Almeida et al. “Discrete and continuum models for the coevolutionary dynamics between CD8+ cytotoxic T lymphocytes and tumour cells.” In: *arXiv preprint arXiv:2109.09568* (2021).

[16] A. Degrassi et al. “Magnetic resonance imaging and histopathological characterization of prostate tumors in TRAMP mice as model for pre-clinical trials.” In: *The Prostate* 67.4 (2007), pp. 396–404.

[17] B. A. Foster et al. “Characterization of Prostatic Epithelial Cell Lines Derived from Transgenic Adenocarcinoma of the Mouse Prostate (TRAMP) Model.” In: *Cancer Research* 57 (Aug. 1997), pp. 3325–3330.

[18] R. Michelini et al. "Vaccine-Instructed Intratumoral IFN-γ Enables Regression of Autochthonous Mouse Prostate Cancer in Allogeneic T-Cell Transplantation." In: *Cancer research* 73 (June 2013).

[19] R. Siegel et al. "Cancer statistics, 2014." In: *CA: a cancer journal for clinicians* 64.1 (2014), pp. 9–29.

[20] M. Malvezzi et al. "European cancer mortality predictions for the year 2013." In: *Annals of Oncology* 24.3 (2013), pp. 792–800.

[21] R. H. Michelini et al. "Concomitant tumor and minor histocompatibility antigen–specific immunity initiate rejection and maintain remission from established spontaneous solid tumors." In: *Cancer research* 70.9 (2010), pp. 3505–3514.

[22] A. R. Elia et al. "Targeting tumor vasculature with TNF leads effector T cells to the tumor and enhances therapeutic efficacy of immune checkpoint blockers in combination with adoptive cell therapy." In: *Clinical Cancer Research* 24.9 (2018), pp. 2171–2181.

[23] T. Manzo et al. "T cells redirected to a minor histocompatibility antigen instruct intratumoral TNFα expression and empower adoptive cell therapy for solid tumors." In: *Cancer research* 77.3 (2017), pp. 658–671.

[24] J. R. Gingrich and N. M. Greenberg. "A transgenic mouse prostate cancer model." In: *Toxicologic pathology* 24.4 (1996), pp. 502–504.

[25] N. M. Greenberg et al. "Prostate cancer in a transgenic mouse." In: *Proceedings of the National Academy of Sciences* 92.8 (1995), pp. 3439–3443.

[26] S. B. Shappell et al. "Prostate pathology of genetically engineered mice: definitions and classification. The consensus report from the Bar Harbor meeting of the Mouse

Models of Human Cancer Consortium Prostate Pathology Committee." In: *Cancer research* 64.6 (2004), pp. 2270–2305.

[27] X. Zheng et al. "Clonal deletion of simian virus 40 large T antigen-specific T cells in the transgenic adenocarcinoma of mouse prostate mice: an important role for clonal deletion in shaping the repertoire of T cells specific for antigens overexpressed in solid tumors." In: *The Journal of Immunology* 169.9 (2002), pp. 4761–4769.

[28] Y. Niu et al. "Tissue prostate-specific antigen facilitates refractory prostate tumor progression via enhancing ARA70-regulated androgen receptor transactivation." In: *Cancer research* 68.17 (2008), pp. 7110–7119.

[29] A.Y. Chuang et al. "Immunohistochemical differentiation of high-grade prostate carcinoma from urothelial carcinoma." In: *The American journal of surgical pathology* 31.8 (2007), pp. 1246–1255.

[30] E. Degl'Innocenti et al. "Peripheral T cell tolerance occurs early during spontaneous prostate cancer development and can be rescued by dendritic cell immunization." In: *European journal of immunology* 35.1 (2005), pp. 66–75.

[31] A. M. Miller and P. Pisa. "Tumor escape mechanisms in prostate cancer." In: *Cancer Immunology, Immunotherapy* 56.1 (2007), pp. 81–87.

[32] H. Garcke et al. "A Cahn-Hilliard-Darcy model for tumour growth with chemotaxis and active transport." In: *Mathematical Models and Methods in Applied Sciences* 26 (Aug. 2016), pp. 1095–1148.

[33] D. Lee et al. "Physical, mathematical, and numerical derivations of the Cahn–Hilliard equation." In: *Computational Materials Science* 81 (2014), pp. 216–225.

[34] A. Agosti et al. “A computational framework for the personalized clinical treatment of glioblastoma multiforme.” In: *ZAMM-Journal of Applied Mathematics and Mechanics/Zeitschrift für Angewandte Mathematik und Mechanik* 98 (May 2018), pp. 2307–2327.

[35] A. Calcinotto et al. “Targeting TNF-α to neoangiogenic vessels enhances lymphocyte infiltration in tumors and increases the therapeutic potential of immunotherapy.” In: *The Journal of Immunology* 188.6 (2012), pp. 2687–2694.

[36] B. He and R. Ganss. “Modulation of the vascular-immune environment in metastatic cancer.” In: *Cancers* 13.4 (2021), p. 810.

[37] C. Slaney, M. Kershaw, and P. Darcy. “Trafficking of T Cells into Tumors.” In: *Cancer Research* 74 (Dec. 2014), pp. 7168–7174.

[38] T. Hillen and K. Painter. “A user’s guide to PDE models for chemotaxis.” In: *Journal of mathematical biology* 58 (Aug. 2008), pp. 183–217.

[39] N. Maimela, S. Liu, and Y. Zhang. “Fates of CD8+ T cells in Tumor Microenvironment.” In: *Computational and Structural Biotechnology Journal* 17 (Nov. 2018).

[40] L.G. De Pillis, A.E. Radunskaya, and C.L. Wiseman. “A Validated Mathematical Model of Cell-Mediated Immune Response to Tumor Growth.” In: *Cancer Research* 65 (2005), pp. 7950–7958.

[41] A. García, J. Seoane, and M. Sanjuán. “On the fractional cell kill law governing the lysis of solid tumors.” In: (Jan. 2016).

[42] A. G. López, J. Seoane, and M. Sanjuán. “A validated mathematical model of tumor growth including tumor-host interaction, cell-mediated immune response and chemotherapy.” In: *Bulletin of Mathematical Biology* 76 (Nov. 2014), pp. 2884–2906.

[43] K. O'Connell et al. "Practical Murine Hematopathology: A Comparative Review and Implications for Research." In: *Comparative medicine* 65 (Apr. 2015), pp. 96–113.

[44] S. Fagerland et al. "Ultrasound and magnetic resonance imaging for group stratification and treatment monitoring in the transgenic adenocarcinoma of the mouse prostate model." In: *The Prostate* 80 (Nov. 2019), pp. 186–197.

[45] E. A. Swabb, J. Wei, and P. M. Gullino. "Diffusion and Convection in Normal and Neoplastic Tissues." In: *Cancer Research* 34 (Oct. 1974), pp. 2814–2822.

[46] A. Puliafito et al. "Three-dimensional chemotaxis-driven aggregation of tumor cells." In: *Scientific Reports* 5 (Oct. 2015), p. 15205.

[47] R. K. Jain. "Transport of molecules in the tumor interstitium: a review." In: *Cancer Research* 47 (June 1987), pp. 3039–3051.

[48] Y. Ji et al. "Stiffness of prostate gland measured by transrectal real-time shear wave elastography for detection of prostate cancer: a feasibility study." In: *The British Journal of Radiology* 92 (Mar. 2019), p. 20180970.

[49] P. Gerlee and A. R. A. Anderson. "An evolutionary hybrid cellular automaton model of solid tumour growth." In: *Journal of theoretical biology* 246(4) (June 2007), pp. 583–603.

[50] H. Frieboes et al. "An Integrated Computational/Experimental Model of Tumor Invasion." In: *Cancer Research* 66 (Mar. 2006), pp. 1597–1604.

[51] F. Vital-Lopez et al. "Modeling the effect of chemotaxis on Glioblastoma Tumor Progression." In: *Aiche Journal - AICHE J* 57 (Mar. 2011).

[52] C. Chatelain et al. “Emergence of microstructural patterns in skin cancer: a phase separation analysis in a binary mixture.” In: *New Journal of Physics* 13 (2011), p. 115013.

[53] A. Matzavinos. “Mathematical modelling of the spatio-temporal response of cytotoxic T-lymphocytes to a solid tumour.” In: *Mathematical Medicine and Biology* 21 (Mar. 2004), pp. 1–34.

[54] A. Logg, G. N. Wells, and J. Hake. “DOLFIN: a C++/Python Finite Element Library.” In: *Automated Solution of Differential Equations by the Finite Element Method, Volume 84 of Lecture Notes in Computational Science and Engineering*. Ed. by Anders Logg, Kent-Andre Mardal, and Garth N. Wells. Springer, 2012. Chap. 10.

[55] M. S. Alnæs et al. “The FEniCS Project Version 1.5.” In: *Archive of Numerical Software* 3.100 (2015).

[56] S. Pieper, M. Halle, and R. Kikinis. “3D Slicer.” In: *2004 2nd IEEE international symposium on biomedical imaging: nano to macro (IEEE Cat No. 04EX821)*. IEEE. 2004, pp. 632–635.

[57] L. Antiga et al. “An image-based modeling framework for patient-specific computational hemodynamics.” In: *Medical & biological engineering & computing* 46.11 (2008), pp. 1097–1112.

[58] G. Tierra and G. Francisco. “Numerical Methods for Solving Cahn-Hilliard Equation and Its Applicability to Related Energy-Based Models.” In: *Archives of Computational Methods in Engineering* 22 (Apr. 2014), pp. 269–289.

[59] D. Kuzmin. “On the design of general-purpose flux limiters for finite element schemes. I. Scalar convection.” In: *Journal of Computational Physics* 219 (Dec. 2006), pp. 513–531.

[60] D. Kuzmin. “Explicit and implicit FEM-FCT algorithms with flux linearization.” In: *Journal of Computational Physics* 228 (Apr. 2009), pp. 2517–2534.

[61] R. Strehl et al. “A Flux Corrected Finite Element Method for Chemotaxis Problems.” In: *Computational Methods in Applied Mathematics* 10 (May 2010), pp. 219–232.

[62] R. Strehl et al. “A positivity-preserving finite element method for chemotaxis problems in 3D.” In: *Journal of Computational and Applied Mathematics* 239 (Jan. 2011), pp. 290–303.

[63] E. Peranzoni et al. “Positive and negative influence of the matrix architecture on antitumor immune surveillance.” In: *Cellular and molecular life sciences* 70.23 (2013), pp. 4431–4448.

[64] E. Lanitis et al. “Mechanisms regulating T-cell infiltration and activity in solid tumors.” In: *Annals of Oncology* 28 (2017), pp. xii18–xii32.

[65] A. Johansson et al. “Tumor-targeted TNFα stabilizes tumor vessels and enhances active immunotherapy.” In: *Proceedings of the National Academy of Sciences* 109.20 (2012), pp. 7841–7846.

MOX Technical Reports, last issues

Dipartimento di Matematica
Politecnico di Milano, Via Bonardi 9 - 20133 Milano (Italy)

05/2022 Aspri, A; Beretta, E.; Cavaterra, C.; Rocca, E.; Verani, M.
Identification of cavities and inclusions in linear elasticity with a phase-field approach

04/2022 Africa, P.C.; Piersanti, R.; Fedele, M.; Dede', L.; Quarteroni, A.
lifex - heart module: a high-performance simulator for the cardiac function

02/2022 Antonietti, P.F.; Scacchi, S.; Vacca, G.; Verani, M.
C^1-VEM for some variants of the Cahn-Hilliard equation: a numerical exploration

03/2022 Giacomini, M.; Perotto, S.
Anisotropic mesh adaptation for region-based segmentation accounting for image spatial information

01/2022 Gavazzoni, M.; Ferro, N.; Perotto, S.; Foletti, S.
Multi-physics inverse homogenization for the design of innovative cellular materials: application to thermo-mechanical problems

95/2021 Di Gregorio, S.; Vergara, C.; Montino Pelagi, G.; Baggiano, A.; Zunino, P.; Guglielmo, M.; Fu
Prediction of myocardial blood flow under stress conditions by means of a computational model

92/2021 Antonietti, P.F.; Manzini, G.; Scacchi, S.; Verani, M.
On arbitrarily regular conforming virtual element methods for elliptic partial differential equations

94/2021 Antonietti, P.F.; Berrone, S.; Busetto, M.; Verani, M.
Agglomeration-based geometric multigrid schemes for the Virtual Element Method

93/2021 Parolini, N.; Dede', L; Ardenghi, G.; Quarteroni, A.
Modelling the COVID-19 epidemic and the vaccination campaign in Italy by the SUIHTER model

87/2021 Both, J.W.; Barnafi, N.A.; Radu, F.A.; Zunino, P.; Quarteroni, A.
Iterative splitting schemes for a soft material poromechanics model